

Ultrafast Photomodulation Spectroscopy: a device-level tool for characterizing the flow of light in integrated photonic circuits

Roman Bruck^{1*}, Ben Mills², Benedetto Troia³, David J. Thomson², Frederic Y. Gardes², Youfang Hu², Goran Mashanovich², Vittorio M. N. Passaro³, Graham T. Reed² and Otto L. Muskens¹

¹*Physics and Astronomy, Faculty of Physical Sciences and Engineering, University of Southampton, Southampton SO17 1BJ, UK*

²*Optoelectronics Research Centre, University of Southampton, Southampton SO17 1BJ, UK*

³*Department of Electrical and Information Engineering, Politecnico di Bari, Via E. Orabona 4, 70125 Bari, Italy*

email: r.bruck@soton.ac.uk

Abstract: Advances in silicon photonics have resulted in rapidly increasing complexity of integrated circuits. New methods are desirable that allow direct characterization of individual optical components in-situ, without the need for additional fabrication steps or test structures. Here, we present a new device-level method for characterization of photonic chips based on a highly localized modulation in the device using pulsed laser excitation. Optical pumping perturbs the refractive index of silicon, providing a spatially and temporally localized modulation in the transmitted light enabling time- and frequency-resolved imaging. We demonstrate the versatility of this all-optical modulation technique in imaging and in quantitative characterization of a variety of properties of silicon photonic devices, ranging from group indices in waveguides, quality factors of a ring resonator to the mode structure of a multimode interference device. Ultrafast photomodulation spectroscopy provides important information on devices of complex design, and is easily applicable for testing on the device-level.

Integrated silicon-based photonics has developed into a mature technology platform with a multitude of applications [1-4], including telecommunications, healthcare diagnostics and optical sensors. As technology progresses, device designs become increasingly complex and integrate more functions onto a single device [5]. Characterization of fabricated devices is an important step in the design cycle as it highlights differences between the intended design

and the fabricated device, thus allowing the optimization of fabrication steps as well as of the entire design process. The toolbox is well filled when it comes to geometrical characterization of waveguides and devices thereof. Established technologies, such as scanning electron microscopy (SEM), atomic force microscopy (AFM), ellipsometry and many others, are able to precisely measure device footprints, waveguide cross sections, surface and sidewall roughness, film thicknesses, and other geometric parameters.

Direct access to properties of light propagation in waveguide devices proves more challenging. Researchers have been inventive and have proposed numerous methods for analysis of integrated optic elements. Among them are reflectometry methods [6-9] to find defects in waveguides, far-field scattering microscopy to measure propagation losses [10-13], as well as interrogation of structures with electron beams (cathodoluminescence) [14], near-field optical probes [14-16], and AFM tips [17-24]. Near-field scanning optical microscopy (NSOM) is a powerful technique that gives direct access to light propagation, including phase information, and features a high spatial resolution [15,16,25,26]. Drawbacks of scanning probe microscopy are the small field of view, slow scanning speeds, and limited reproducibility and durability of the tips. Moreover, near-field techniques require direct access to the waveguide surface in order to interact with evanescent field components, limiting the analysis of devices covered with a top cladding for protection and stability.

Here, we present a new approach for characterization of silicon on insulator (SOI) waveguide elements at the device-level based on non-contact perturbation of the structure using a tightly focused femtosecond laser pulses. The principle of Ultrafast Photomodulation Spectroscopy (UPMS) is shown in Fig. 1. Ultrashort UV laser pulses are focused from the top onto a small area of the device under test (DUT). The pulsed laser excitation produces a highly localized and time-dependent perturbation in the refractive index of silicon, which acts as a local gate for monitoring the flow of probe light through the structure. As the timing and the position of this gate is known, it can be used to reconstruct a space and time dependent photomodulation map of the structure by monitoring the transmission through the device. The technique can be used for devices covered with any top cladding that does not absorb the pump pulses, which includes popular choices such as silicon dioxide and most polymer claddings. Ultrafast response of waveguides was studied earlier in the context of adiabatic frequency conversion and ultrafast switching [27-34]. Collinear infrared pump-probe arrangements have been used to characterize pulse propagation and waveguide nonlinearities [35]. While our setup can also be applied for ultrafast control of SOI elements, we focus here on the imaging and quantitative characterization aspect, which is ideally suited for device performance characterization.

UPMS targets the rapid analysis of optical elements embedded in complex systems consisting of many elements on a single chip. By choosing the position to be pumped, elements within the device can be addressed and analyzed individually, even if their individual transfer functions are obscured by subsequent optical elements. Methods perturbing the near field, would, in principle, deliver a similar kind of information. However, devices developed toward industrial applications, will most likely be covered with a top cladding, and thus do not give access to the near field. Further, alignment tolerances in all three dimensions of the position of incident pump pulses are relaxed compared to the tolerances required for near field probes. UV pumping provides subwavelength resolution for the NIR probe without requiring access to the near-field, which greatly reduces complexity and applicability in realistic device testing environments. Together with the fact that the scanning field of UPMS can be arbitrarily extended in the spatial and time dimensions, UPMS can be easily applied for automated testing of complex optical devices, where pre-programmed positions are analyzed automatically.

Results and Discussion

The UPMS technique provides hyperspectral information which can be independently analyzed as function of four different parameters, namely two coordinates of the pump spot, wavelength and delay time. By moving the objective over the area of the DUT, two dimensional scans of the pump spot on the DUT allow for spatial mapping of the mode distribution similar to AFM-based modulation techniques [19]. The spatial resolution of the UPMS is sub-micrometer, and thus comparable to telecom wavelengths inside high-index waveguides. It is limited by the spot size of the pump pulses, as spatial broadening of the excited spot can be neglected for small delay time (<100ps). Hyperspectral information is obtained by spectrally resolving the transmission spectrum over the bandwidth of the femtosecond probe laser. The probe features a Gaussian spectrum of about 44 nm full-width at half maximum. Because of the high sensitivity of the equipment used, a wider wavelength window into the wings of the pulse spectrum can be analyzed. Typically, wavelength windows of 60 nm to 100 nm width can be achieved. Finally, the delay time, i.e. the timing between the pump and probe pulses, is used to extract information on the time-response of the structures with ultrashort resolution (150 fs).

Characterization of group index modulation. As a first step, we quantified the perturbation in the waveguide group index Δn_g caused by pulsed laser excitation employing an asymmetric Mach-Zehnder interferometer (MZI) as the DUT as shown in Fig. 2a. Pulsed laser excitation in one arm of the MZI resulted in a change in the spectral position and the contrast of the interference fringes of the transmission function (Fig. 2b). Its analysis gives

simultaneous access to the changes in the real and imaginary part of the group index, respectively through the wavelengths shift $\Delta\lambda$ and the fringe contrast (see Methods).

Figure 2c and d display the measured results for Δn_g averaged over a wavelength window of 40 nm width around a center wavelength of 1550 nm. Remarkably, the real part of the group index decreases by more than 0.4 without any visible damage to the waveguide. As a result, phase shifts greater than 2π are obtained over a modulated zone of only a few optical wavelengths in length. Some saturation is observed for the change in the real part at high laser powers. For large negative delay times (not shown in Fig 2d), the real part of Δn_g decays exponentially with a time constant of roughly 300 ps (± 70 ps) for the rib waveguides under investigation. The modulation of the imaginary part of the group index, responsible for the induced absorption, increases much less than the real part and shows a linear behaviour as function of the pump fluence.

The index modulation in our experiment is attributed to free carrier contributions. Free carrier nonlinearity is caused by formation of electron-hole pairs and provides a reduction of the refractive index and an increase in absorption [36]. The pump fluence of $100 \text{ pJ}/\mu\text{m}^2$ has been shown before to result in electron-hole pair densities exceeding 10^{20} cm^{-3} [37], for which the free carrier nonlinearity of Si [36] predicts a refractive index modulation of $\Delta n_{\text{Si}} = -0.173 + 10^{-4}i$, corresponding to $\Delta n_g = -0.242 + 10^{-4}i$ in our waveguides. Our values for the real part of Δn_g are in agreement with these high carrier densities. For long delay times ($>20\text{ps}$), we expect the imaginary part to follow this prediction as well and decay with the same time constant as the real part. Measurements of imaginary parts in the range of 10^{-4} , however, are beyond the sensitivity limits of our experiment. For short time delays, higher values than predicted are found for the imaginary part of Δn_g . This transient increase in absorption is attributed to hot carriers generated by the pulsed UV excitation, which increase the damping rate through electron-electron collisions [37,38]. This transient contribution relaxes over several picoseconds to levels expected for the conventional free carrier nonlinearity. Additionally, the presence of surface states in the etched SOI waveguides may result in additional defect-related contributions to absorption and differences in carrier dynamics. Our results are in qualitative agreement with previous studies on switching of Si photonic crystal membranes, which also identified free carrier effects as the dominant contribution [29,30]. Those studies were done at lower pump intensities, resulting in smaller values of Δn . The low repetition rate in our studies resulted in a negligible thermo-optic background, therefore we have good access to events occurring at negative delay times, i.e. when probe pulses arrive before the pump pulses. This feature is important for time-resolved investigation of resonator elements as will be

shown below. The dynamics of the recovery process is governed by relaxation and transverse diffusion of excited carriers. Transverse diffusion causes spatial broadening of the area of effect. We quantified in our experiments that the effect length increases by 500 nm over 100 ps, corresponding to a lateral diffusion constant of around $1 \text{ cm}^2/\text{s}$ (see Methods). For measurements on timescales of maximum tens of picoseconds, this expansion of the excited spot can therefore be neglected and the resolution is set by the optical excitation area.

Group index dispersion of a waveguide. UPMS allows direct measurements of the group index and its dispersion on any SOI waveguide by precise time of flight measurements using excitation of the waveguide as an ultrafast nonlinear gate (Fig. 3a). So far, group index measurements have been performed on specially designed test elements, such as asymmetric MZIs [40], where the group index has been deduced from transmission spectra. Other approaches used the spectra of Fabry-Perot resonances in cavities [41-43], time of flight measurements using an external Kerr shutter [44], or direct measurements employing NSOM [15]. UMPS gives access to the spectrally resolved change of transmission ($\Delta T/T$) as displayed in Fig. 3b for a position 1.8 mm from the beginning of the investigated waveguide. For positive delay times, dark colours indicate a decrease in transmission due to absorption. Probe light arriving before the pump excitation, i.e. at negative delay times, is not modulated, resulting in a sharp step edge in the modulation time response. The pump-probe map shows two step edges, corresponding to TE and TM polarized light. The latter is weakly confined to the waveguide, and contributes significantly in our experiment only in a limited spectral range around the centre wavelength of the probe. Due to group index dispersion, the arrival time of the probe light is a function of wavelength and the step edges are not vertical. By following the absolute position and the evolution of the slope of the step edge over the length of the waveguide (Fig. 3c,d) the group index and its linear dispersion can be calculated. Since only the evolution of the slope and not the absolute slope of the step edge is analyzed along the waveguide, this technique is not sensitive to chirp in the incident probe pulses. The resulting group index dispersions are shown in Fig. 3e and f for the TE and TM polarization components respectively (blue lines). Good agreement is obtained with numerical results based on finite element method (FEM) simulations (red lines), with the small systematic shift in TM most likely representing a difference in precise design geometry. Our measurements are also in agreement with the work of Dulkeith et al., who investigated comparable waveguides [45].

Time response of a ring resonator. Typically, quality factors of ring resonators are obtained from the linear transmission spectrum using the equation $Q = f/\Delta f$ on the dips in transmission (e.g. [46-48]). However, closer to the

fundamental definition of the Q-factor as the ratio of energy stored to energy dissipated per cycle, are measurements in the time-domain. On resonance, light from the bus waveguide is coupled into the ring with high efficiency and is stored over many cycles before leaking back to the output waveguide. The corresponding delay time can be detected by UPMS using a negative delay time, i.e. probe pulses arriving at a time before the pump pulses. In this case, only light stored in the ring resonator for at least the delay time is affected by the excitation and the corresponding photomodulation response will be a measure of the amount of energy stored in the ring. For long negative times, an exponentially decaying UPMS effect is expected, as less and less light from the ring transfers back to the bus waveguide.

For analyzing the ring resonator, a spot on the bus waveguide, shortly after the ring resonator (see Fig. 4a) is excited. The time response of the unperturbed ring resonator is modelled as a carrier frequency with exponentially decaying envelope as indicated by the black dashed line in Fig. 4b resulting in a single Lorentzian resonance. Photomodulation is subsequently included by suppressing the transmission after a time corresponding to the negative delay time of Fig. 4b. After Fourier transformation, this truncation produces a characteristic ripple in the frequency spectrum, as is shown in the differential $\Delta T/T$ response in Fig. 4c

Figure 4d shows the experimentally obtained $\Delta T/T$ for the ring resonator as function of delay time and wavelength. The resonances of the ring are clearly visible in the graph at negative delay times. As only the bus waveguide is pumped, the ring itself is undisturbed and no shift in the cavity resonance is observed. Similar to the straight waveguide, the zero timing slightly depends on the wavelength due to group index dispersion in the bus waveguide. Figure 4e represents cuts through the graph in Fig. 4b at the resonance wavelength of 1527.7 nm for delay times between -5 ps and -2 ps. We find the symmetric sidebands around the resonance wavelength as predicted by the analytical model. In order to obtain the cavity ringdown time, we plotted in Fig. 4f the modulation amplitude at the resonance wavelength versus delay time. A response of $\frac{\Delta T}{T} \sim -e^{-\frac{t}{\tau}}$, with an exponential decay time τ , was observed for long negative delay times beyond -4 ps. The different resonances of the ring within the spectral range of our setup were analyzed and corresponding Q factors are presented in a histogram in the inset of Fig. 4f (blue bars). Values of Q-factors in the range 1000 to 2000 are observed, which are of the same order as Q-factors obtained from optical transmission spectra of the same device using a narrowband telecom setup (orange bars). Quality factor measurements obtained directly from the transmission spectrum are susceptible to intensity noise, reflections on interfaces or any defects/deviations in the device contaminating the transmission spectrum, which

particularly for the end-face coupling used in our experiments limits the accuracy of this method. In comparison, time-domain UPMS offers a more direct way of determining the Q-factor through the characteristic decay time of the resonance modulation. UPMS time domain measurements are only limited by the optical path delay, allowing, in principle, for characterization of Q-factors up to 10^6 with standard nanosecond delay lines.

Resonances of Vernier racetracks. Devices exploiting the Vernier-effect are composed of two resonators with similar, but slightly different lengths. Such devices are interesting for sensing applications [49] and particularly challenging to characterize because the resonators are designed with overlapping resonances, where the degree of overlap depends on the wavelength. Further, their long lengths result in a small free spectral range (FSR). Transmission measurements do not allow the characterization of the individual resonators as the light travels through both resonators and only the combined transmission function is accessible. For UPMS characterization of Vernier racetracks (see Fig. 5a), we excited a spot directly on each racetrack. Figure 5b shows a photograph of the setup and the sample employing grating couplers for in- and outcoupling from and to single mode fibers. The UPMS measurements of the two racetracks are presented in Fig. 5c and d. For positive delay times, the optical length of the resonators is altered as the resonators are excited directly, thus shifting the resonance wavelengths. For negative delay times, behaviour similar to the ring resonator in Figure 4 is found, however, with a smaller FSR. Thus, for each resonator individually, the resonance wavelengths but also the corresponding Q-factors can be extracted employing the methods presented above for the ring resonator. Additionally, the different round trip times of the resonators show clearly in the UPMS signal if integrated over the available wavelength (Fig. 5e). Figure 5f shows a transmission measurement of the investigated device and the UPMS signal for both resonators at a delay time of -1 ps. From these data, resonance wavelengths found for the combined system from the transmission measurements and for the individual rings by UPMS were extracted and are presented in Fig. 5g. The FSRs of the racetracks were calculated as 1.84 nm and 1.76 nm at 1.55 μm for the first and the second resonator, respectively. Many devices with subsequent or cascaded elements would be similarly difficult to analyse by transmission measurements. A common example would be subsequent ring resonators as multiple drop filters in telecommunication applications. In complex devices, the drop ports might not be directly accessible and the transmission function cannot attribute individual dips in the spectrum to the corresponding resonator. This information is easily accessible employing UPMS.

Mapping of a multimode interference (MMI) splitter. We use UPMS to investigate the spatial distribution of light involved in the transport from the input to one of the output waveguides in an MMI. In MMI-devices, a complex mode pattern defines how light is coupled to the output waveguides. By introducing a localized modulation in the MMI-region, the contribution of an excited spot to the selected output can be altered, and thus identified. Generally, two effects will be induced by the laser excitation: (i) rerouting of light from one output to the other and (ii) localized suppression of transmission due to absorption or scattering. Figure 6a shows an SEM image of the MMI device under study. As shown in the left part of Fig. 6b, the field distribution in the symmetric 50/50 splitter device calculated by finite-difference time domain (FDTD) simulations shows a symmetric profile. However, the distribution contributing to only one of the two outputs is asymmetric, as can be appreciated by looking at the time-reversed situation, i.e. light launched from one of the two inputs (right part of Fig. 6b). In contrast to NSOM, which provides the symmetric mode intensity, UPMS selectively provides specific information on the light paths involved in the light transport to the detection point. Figure 6d,e show photomodulation maps corresponding to the transmission measured at the lower and upper output waveguides, respectively, at a wavelength of 1556.5 nm. Blue regions correspond to the case of reduced transmission. Comparison with the time-reversed asymmetric profile of Fig. 6b shows strong similarities between the regions of suppressed transmission and high intensity paths. Next to regions of reduced transmission, regions are observed where the transmission is enhanced. These red areas correspond to parts of the mode profile where the contribution to the selected output can be increased. For such regions, the induced change in Δn_{Si} redirects light from one waveguide to the other waveguide. As the average magnitude of blue areas is significantly larger than for red areas, a major contribution to the reduction in transmission for blue areas can be attributed to induced absorption and scattering of light out of individual lightpaths. For rerouting of light, similar magnitudes for red and blue areas would be expected.

Conclusions

We have developed a new technique of ultrafast photo-modulation spectroscopy (UPMS). This technique offers a multidimensional, hyperspectral characterization for silicon waveguide based elements at the device level. By introducing a localized modulation in the refractive index of silicon employing a short pump wavelength of 400 nm, light propagation in silicon photonic elements can be altered and identified with a spatial resolution that compares with telecommunication wavelengths inside the high-index structures. A decrease in the group index due to optical pumping larger than 0.4 in the real part and an increase of up to 0.06 in the imaginary part is obtained at medium

pump fluences of around $100 \text{ pJ}/\mu\text{m}^2$, without inducing any damage to the silicon nanophotonic elements. This large modulation of the real part of the group index on a time scale of picoseconds is of interest for active control of nanophotonic devices, which will be explored in future work. UPMS provides access to time-domain measurements and allows for simultaneous spatial and spectral mapping. Compared to scanning near-field techniques, the far-field excitation is robust and can be used in the presence of transparent cladding layers. We have demonstrated the use of UPMS in silicon photonics, however, we expect the technique to be generally applicable to other types of semiconductor integrated photonics platforms, as well as to other materials such as metals with potential application in plasmonics. We have demonstrated the versatility for imaging and quantitative analysis of essential components such as MZIs, waveguides, ring resonators, and MMI devices. While we have focused here on the characterization aspects, the high modulation effects UPMS can also be used to efficiently modulate silicon nanophotonic devices on length scales of only a few optical wavelengths, facilitating further developments toward reconfigurable integrated circuits with small footprints.

Methods

Optical setup. The laser system used for the presented measurements is a Ti-Sapphire laser coupled with an optical parametric amplifier giving 150 fs pulses at a 250 kHz repetition rate. It provides an output for 400 nm pump pulses and an output of variable wavelength (visible range to $2 \mu\text{m}$) for probe pulses. All presented measurements used a central wavelength of 1550 nm for the probe pulses and TE-polarization. In our setup (see Fig. 1) the probe pulses are coupled by a microscope objective into an input waveguide. The transmitted light of one output of the DUT is coupled into a fibre and subsequently to a spectrometer. The pump pulses can be focused from the top onto any position of the DUT.

Mach-Zehnder Interferometer. The asymmetric MZI is composed from rib waveguides (450 nm width, 220 nm total thickness, 100 nm slab thickness, silicon dioxide as lower and top cladding). The short arm of the MZI has a length of around $1040 \mu\text{m}$, the long arm is $180 \mu\text{m}$ longer. While this path length difference is longer than the length of the femtosecond pulses, it is much less than the millimeter coherence length associated with the spectrometer resolution, therefore clear interference fringes were obtained in the transmission spectrum. Changes in the real part of the effective index $\text{Re}(\Delta n_g)$ were obtained from the fringe shift $\Delta\lambda$ through the relation $\text{Re}(\Delta n_g)L_p = \frac{\lambda}{\lambda_{FSR}}\Delta\lambda$, with the free spectral range given by $\lambda_{FSR} = \frac{\lambda^2}{n_g \Delta L}$. Here, n_g denotes the group index,

λ the wavelength in vacuum and ΔL the length difference between the arms of the MZI. The spectral shift $\Delta\lambda$ was calculated for each fringe individually. The values given in Fig 2c,d for the real part are the mean values of this set of numbers, while the error bars denote the standard deviation. The pumping length L_p corresponds to the length of the pumped section of the waveguide, where we assumed a homogeneous pumping intensity. The change in the imaginary part of Δn_g was obtained from the amplitude of the interference fringes with (A') and without (A) pumping through the relation $\text{Im}(\Delta n_g)L_p = -\frac{\lambda}{2\pi} \ln \frac{A'}{A}$. After compensating for the Gaussian spectrum of the probe pulses, the amplitudes A' and A were obtained from sine-fits to the fringe pattern over a 40 nm wide wavelength window. The error bars given in Fig. 2c,d for the imaginary part were deducted from the 95% confidence levels of those fits. Two measurements with different pump pulse spot diameters were performed, corresponding to $L_p=1.5 \mu\text{m}$ and $3.5 \mu\text{m}$. The pumping lengths were adjusted by defocusing the microscope objective and were measured by lateral scans over the waveguide. We calculated the effect lengths as the full width at 1/e maximum of a Gaussian fit to the lateral scans minus the width of the waveguide. The thick solid lines in Fig. 2c denote a linear fit for the imaginary part and a fit of $\text{Re}(\Delta n_g) = c \frac{p}{p+s}$ for the real part, with scaling factor c and saturation parameter $S = 346 \pm 300 \text{ pJ}/\mu\text{m}^2$. For the measurements presented in Fig. 2d, a pump fluence of $130 \text{ pJ}/\mu\text{m}^2$ was used. Pump fluences were measured before the pump beam entered the focusing objective. From the measured transverse expansion of $2R=500\text{nm}$ over 100ps we assumed a diffusive process with r.m.s. broadening radius given by $R=(6Dt)^{1/2}$. Thus, the diffusion constant D is given by $D=R^2/6t$ resulting in about $D=1 \text{ cm}^2/\text{s}$.

Waveguide. The group index measurements were performed on a straight wire waveguide (470 nm width, 220 nm thickness, silicon dioxide lower cladding and air as top cladding) of about 4 mm length. The error bars in Fig. 3e,f are 95% confidence levels for the linear fits on the measured step edge positions and slopes. For the numerical calculation of the group index, the waveguide cross section of the waveguide (see inset in Fig. 3a) was measured using SEM and implemented in the FEM model. For group index measurements the pump fluence was set to $96 \text{ pJ}/\mu\text{m}^2$. A running average of $\pm 75 \text{ nm}$ in time axis was employed on the graph presented in Fig. 3b). This averaging is on the time scale of the exciting pump pulses, thus no physical relevant features are expected to be lost. A similar running average was employed on all UPMS measurements that are plotted as function of delay time.

Ring resonator. The ring resonator and the bus waveguide are made from identical waveguides as the MZI. A pump fluence of $64 \text{ pJ}/\mu\text{m}^2$ was employed. The decay time of the ring resonator was obtained using exponential

fitting of the (negative) modulation amplitude at resonance for PPTDs between -10 ps and -4 ps (in this range single-exponential decay was observed). The time constant τ of this exponential decay was converted to the Q-factor using the relation [50]:

$$Q = \frac{2\pi c\tau}{\lambda} \quad (1)$$

The error bars given for the Q-factors in the inset in Fig. 4f are based on 95% confidence levels of the exponential fits.

Vernier racetracks. The racetrack resonators and waveguides are composed from rib waveguides (450 nm width, 400 nm total thickness, 180 nm slab thickness, silicon dioxide as lower and air as top cladding). The first racetrack has a length of 328 μm with a 10 μm straight coupling region, the length of the second racetrack is 345.2 μm with a 9.2 μm long straight coupling region. A pump fluence of 96 pJ/ μm^2 was used. The resonance wavelengths presented in Fig 5f) were extracted from the UPMS measurements presented in Fig. 5f). The resonance wavelengths correspond to the minima of the UPMS spectrum.

Multimode interference device. Spatial maps of the MMI were obtained for both output waveguides by translating the output fibre to pick up light from the individual outputs. In this way, the symmetry of the device was proven to good agreement. Maps of the MMI for various input conditions were calculated using the Lumerical FDTD package. In the MMI experiments, a pump fluence of 96 pJ/ μm^2 was used.

References

- [1] Soref, R. Silicon Photonics: A Review of Recent Literature. *Silicon* **2**, 1–6 (2010).
- [2] Passaro, V.M.N. et al. Recent Advances in Integrated Photonic Sensors. *Sensors* **12**, 15558-15598 (2012).
- [3] Jalali, B. & Fathpour, S. Silicon Photonics. *J. of Lightw. Techn.* **24**, 4600-4614 (2006).
- [4] Yamada, K. et al. High-performance silicon photonics technology for telecommunications applications. *Sci. Technol. Adv. Mater.* **15**, 024603 (2014).
- [5] Kuramochi et al., Large-scale integration of wavelength-addressable all-optical memories on a photonic crystal chip, *Nature Photon.* **8**, 474–481 (2014).
- [6] Beaud, P. et al. Optical Reflectometry with Micrometer Resolution for the Investigation of Integrated Optical Devices. *J. Quant. El.* **25**, 755-759 (1989).
- [7] Youngquist, R.C., Carr, S., & Davies D.E.N. Optical coherence-domain reflectometry: a new optical evaluation technique. *Opt. Lett.* **12**, 158-160 (1987).
- [8] Kohlhaas, A., Frömchen, C. & Brinkmeyer, E. High-Resolution OCDR for Testing Integrated-Optical Waveguides: Dispersion-Corrupted Experimental Data Corrected by a Numerical Algorithm. *J. Lightw. Techn.* **9**, 1493-1502 (1991).
- [9] Glombitza, U. & Brinkmeyer, E. Coherent Frequency-Domain Reflectometry for Characterization of Single-Mode Integrated-Optical Waveguides. *J. Lightw. Techn.* **11**, 1377-1384 (1993).

- [10] Loncar, M. et al. Experimental and theoretical confirmation of Bloch-mode light propagation in planar photonic crystal waveguides. *Appl. Phy. Lett.* **80**, 1689-1691 (2002).
- [11] McNab, S.J., Moll, N. & Vlasov, Y.A. Ultra-low loss photonic integrated circuit with membrane-type photonic crystal waveguides. *Opt. Ex.* **22**, 2927-2939 (2003).
- [12] Hopman, W.C.L., Hoekstra, H.J.W.M., Dekker, D., Zhuang, L. & de Ridder, R.M. Far-field scattering microscopy applied to analysis of slow light, power enhancement, and delay times in uniform Bragg waveguide gratings. *Opt. Ex.* **15**, 1851-1870 (2007).
- [13] García, P.D., Smolka, S., Stobbe, S. & Lodahl, P. Density of states controls Anderson localization in disordered photonic crystal waveguides. *Physical Review B* **82**, 165103 (2010).
- [14] Sapienza, R. et al. Deep-subwavelength imaging of the modal dispersion of light. *Nature Materials* **11**, 781-787 (2012).
- [15] Gersen, H., et al. Real-space observation of ultraslow light in photonic crystal waveguides. *Phys. rev. let.* **94**, 073903 (2005).
- [16] Engelen, R.J.P. et al. Ultrafast evolution of photonic eigenstates in k-space. *Nature Physics* **3**, 401-405 (2007).
- [17] Kramper, P. Near-field visualization of light confinement in a photonic crystal microresonator. *Opt. Lett.* **29**, 174-176 (2004).
- [18] Koenderink, A.F., Kafesaki, M., Buchler, B.C. & Sandoghdar, V. Controlling the Resonance of a Photonic Crystal Microcavity by a Near-Field Probe. *Phys. Rev. Lett.* **95**, 153904 (2005).
- [19] Märki, I., Salt, M., Herzig, H. P. Tuning the resonance of a photonic crystal microcavity with an AFM probe. *Opt. Exp.* **14**, 2969-2978 (2006).
- [20] Hopman, W.C.L. et al. Nano-mechanical tuning and imaging of a photonic crystal micro-cavity resonance. *Opt. Exp.* **14**, 8745-8752 (2006).
- [21] Robinson, J.T., Preble, S.F., Lipson, M. Imaging highly confined modes in sub-micron scale silicon waveguides using Transmission-based Near-field Scanning Optical Microscopy. *Opt. Exp.* **14**, 10588-10595 (2006).
- [22] M. Burrese et al., Magnetic Light-Matter Interactions in a Photonic Crystal Nanocavity. *Phys. Rev. Lett.* **105**, 123901 (2006).
- [23] L. Lalouat et al., Near-field interactions between a subwavelength tip and a small-volume photonic-crystal nanocavity. *Phys. Rev. B* **76**, 041102(R) (2007).
- [24] W.C.L. Hopman et al., Nano-mechanical tuning and imaging of a photonic crystal micro-cavity resonance. *Opt. Ex.* **14**, 8745- 8752 (2006).
- [25] Burrese, M. et al. Probing the Magnetic Field of Light at Optical Frequencies. *Science* **326**, 550-553 (2009).
- [26] Gersen, H., Korterik, J.P., van Hulst, N.F. & Kuipers, L. Tracking ultrashort pulses through dispersive media: Experiment and theory. *Phys. Rev. E* **68**, 026604 (2003).
- [27] Beggs, D.M. et al. Ultrafast Tunable Optical Delay Line Based on Indirect Photonic Transitions. *Phys. Rev. Lett.* **108**, 213901 (2012).
- [28] Beggs, D.M., Krauss, T.F., Kuipers, L., & Kampfrath, T. Ultrafast Tilting of the Dispersion of a Photonic Crystal and Adiabatic Spectral Compression of Light Pulses. *Phys. Rev. Lett.* **108**, 033902 (2012).
- [29] Opheij, A. et al. Ultracompact (3 μm) silicon slow-light optical modulator. *Scientific Reports* **3**, 3546 (2013).
- [30] Liang, T.K. et al. Ultrafast nonlinear optical studies of silicon nanowaveguides. *Opt. Exp.* **13**, 7298-7303 (2005).
- [31] Slavik, R., Park, Y., Kulishov, M., Morandotti, R. & Azana, J. Ultrafast all-optical differentiators. *Opt. Exp.* **14**, 10699-10707 (2006).
- [32] Preble, S.F., Xu, Q., Schmidt, B.S. & Lipson M. Ultrafast all-optical modulation on a silicon chip. *Opt. Lett.* **30**, 2891-2893 (2005).
- [33] Upham, J. et al The capture, hold and forward release of an optical pulse from a dynamic photonic crystal nanocavity. *Opt. Exp.* **21**, 3809-3817 (2013).
- [34] Kondo, K. et al. Ultrafast Slow-Light Tuning Beyond the Carrier Lifetime Using Photonic Crystal Waveguides, *Phys. Rev. Lett.* **110**, 053902 (2013).
- [35] Motamedi, A.R., Nejadmalayeri, A.H., Khilo, A., Kärtner, F.X. & Ippen, E. P. Ultrafast nonlinear optical studies of silicon nanowaveguides. *Opt. Exp.* **20**, 4085-4101 (2012).
- [36] Soref, R.A. & Bennett, B. R. Electrooptical effects in silicon. *IEEE J. Quant. Electr.* **23**, 123-129 (1987).
- [37] Sokolowski-Tinten, K., von der Linde, D., Generation of dense electron-hole plasmas in silicon. *Phys. Rev. B* **61**, 2643-2650 (2000).
- [38] Sabbah, A. J., & Riffe, D. M. (2002). Femtosecond pump-probe reflectivity study of silicon carrier dynamics. *Phys. Rev. B* **66**, 165217 (2002).
- [39] Kampfrath, T. et al. Ultrafast rerouting of light via slow modes in a nanophotonic directional coupler. *Appl. Phys. Lett.* **94**, 241119 (2009).

- [40] Vlasov, Y.A., O'Boyle, M., Hamann, H.F. & McNab, S.J. Active control of slow light on a chip with photonic crystal waveguides. *Nature* **483**, 65-69 (2005).
- [41] Letartre, X. et al. Group velocity and propagation losses measurement in a single-line photonic-crystal waveguide on InP membranes. *Appl. Phys. Lett.* **79**, 2312-2314 (2001).
- [42] Lee, M.W. et al. Characterizing photonic crystal waveguides with an expanded k-space evanescent coupling technique. *Opt. Ex.* **16**, 13800-13808 (2008).
- [43] Notomi, M. et al. Extremely Large Group-Velocity Dispersion of Line-Defect Waveguides in Photonic Crystal Slabs. *Phys. Rev. Lett.* **87**, 253902 (2001).
- [44] Finlayson, C.E. et al. Slow light and chromatic temporal dispersion in photonic crystal waveguides using femtosecond time of flight. *Phys. Rev. E* **73**, 016619 (2006).
- [45] Dulkeith, E., Xia, F., Schares, L., Green, W.M.J. & Vlasov, Y.A. Group index and group velocity dispersion in silicon-on-insulator photonic wires. *Opt. Ex.* **14**, 3853-3863 (2006).
- [46] Niehusmann, J. et al. Ultrahigh-quality-factor silicon-on-insulator microring resonator. *Opt. Lett.* **29**, 2861-2863 (2004).
- [47] Baehr-Jones, T., Hochberg, M., Walker, C. & Scherer, A. High-Q optical resonators in silicon-on-insulator-based slot waveguides. *Appl. Phys. Lett.* **86**, 081101 (2005).
- [48] Almeida, V.R., Barrios, C.A., Panepucci, R.R. & Lipson, M. All-optical control of light on a silicon chip. *Nature* **431**, 1081-1084 (2004).
- [49] Passaro, V.M.N., Troia, B. & De Leonardi, B., A generalized approach for design of photonic gas sensors based on Vernier-effect in mid-IR. *Sensors and Actuators B* **168**, 402-420 (2012).
- [50] Xu, Q. & Lipson, M. All-optical logic based on silicon micro-ring resonators. *Opt. Ex.* **15**, 924-929 (2007).

Acknowledgements

The authors acknowledge support from EPSRC through grant no. EP/J016918.

Author contributions

R.B. and O.L.M developed the UMPS setup, R.B. performed the presented experiments. Data analysis and theoretical background was done by R.B. and O.L.M.. B.M. was responsible for the laser system and contributed in the development of the setup. D.J.T., F.Y.G., Y.H., G.M. and G.T.R. designed and fabricated the characterized samples in Figures 2, 4, and 6. B.T. and V.N.M.P. designed and fabricated the sample characterized in Fig. 5. R.B. and O.L.M wrote the paper in consultation with all the authors.

Competing financial interests

The authors declare no competing financial interests.

Figure captions

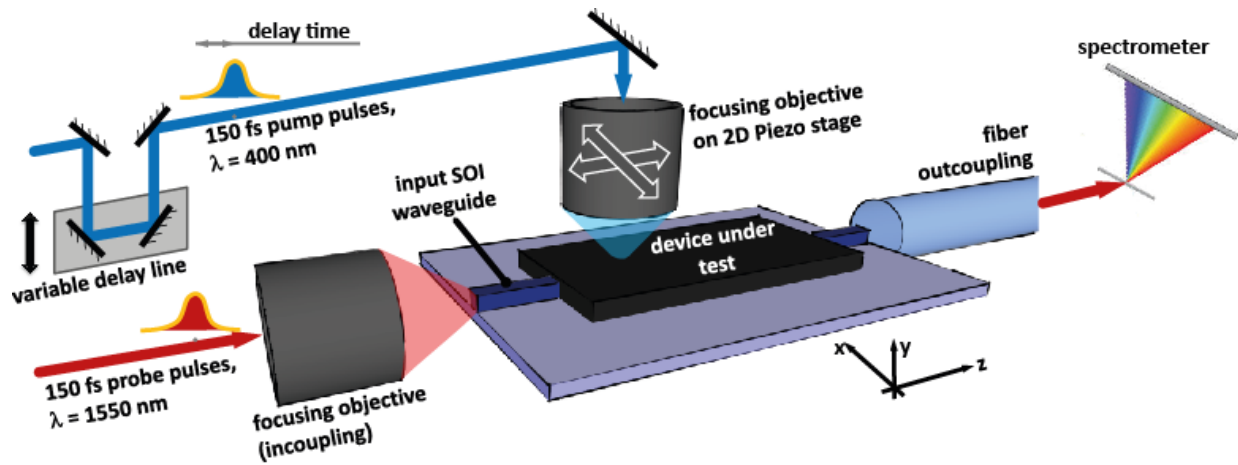


Fig. 1. Schematic of the UPMS setup. Infrared probe pulses are coupled into a SOI waveguide, travel through the device-under-test and are outcoupled to a singlemode fiber. The transmission is spectrally resolved in a spectrometer. Pump pulses are incident on the device region from the top. The incident position of the pump pulses can be scanned over the device and the delay time can be adjusted.

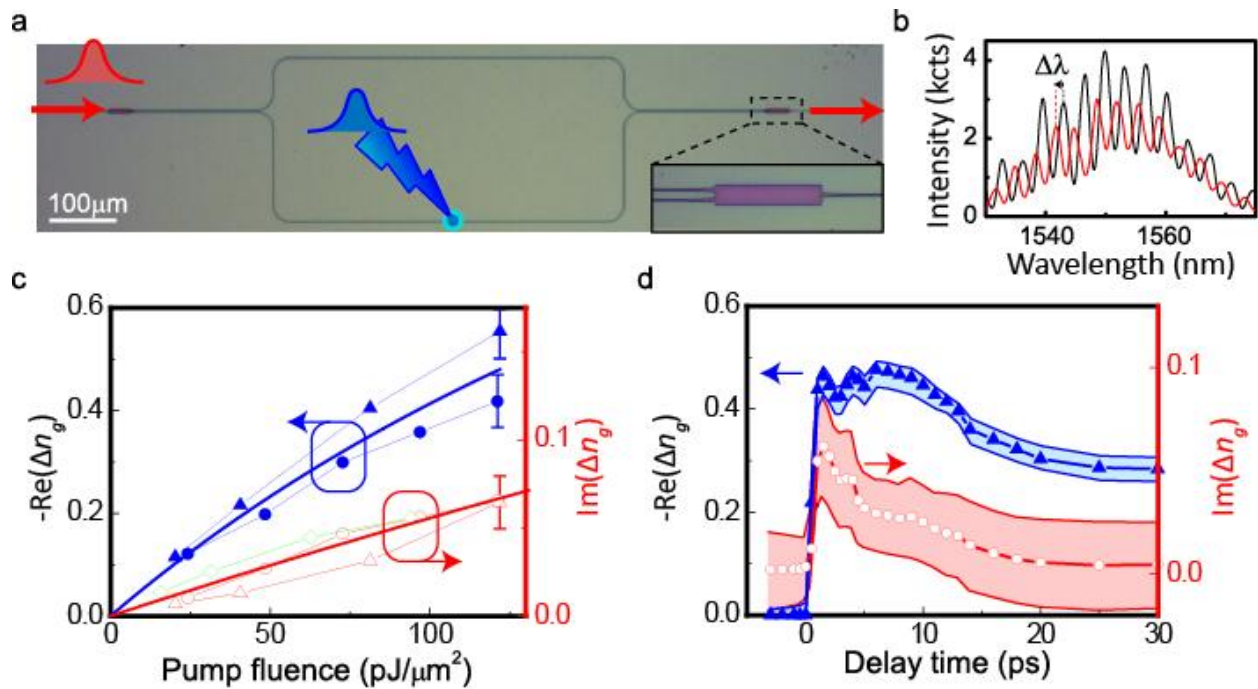


Fig. 2. Quantification of the complex group index change. a) Asymmetric Mach-Zehnder interferometer (MZI) used to determine the group index change induced in the waveguide by the UV pump pulses. b) Transmission spectra (unit kilo-counts) of the unpumped (black) and pumped (red) MZI, showing shift $\Delta\lambda$ of interference fringes and reduced fringe contrast due to absorption. c) Measured change of the real (blue) and imaginary (red) part of the group index as function of the pump fluence, for two effect lengths of 1.5 μm (dots) and 3.5 μm (triangles) and a delay time of 5 ps. Green diamonds are direct measurements of absorption through intensity

modulation of a straight waveguide. Lines are guides to the eye using linear saturation equation (see Methods). d) Change in the real (blue) and imaginary (red) part of the group index as function of delay time (pump fluence $130 \text{ pJ}/\mu\text{m}^2$, $1.3 \text{ }\mu\text{m}$ effect length).

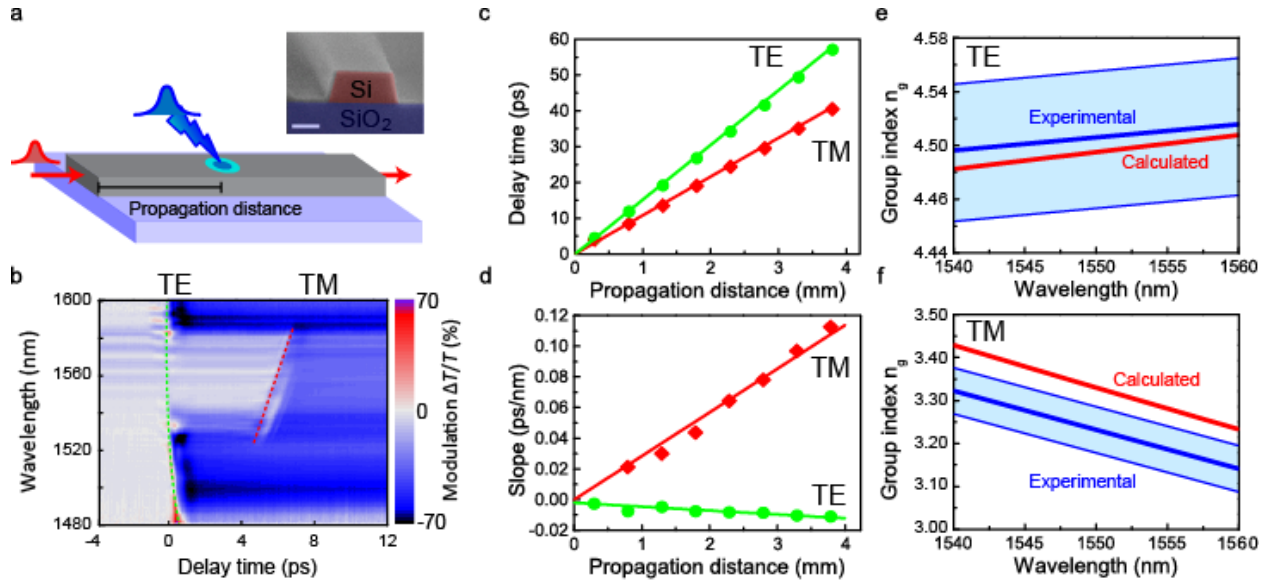


Fig. 3. Group index measurements. a) Schematic of the experiment using excitation of a single-mode waveguide (SEM image in inset, scale bar 200 nm). b) Delay time scan for a straight waveguide, performed 1.8 mm from waveguide beginning (Zero delay time in this scan chosen for clarity as the arrival time of the TE light). Red and green dashed lines correspond to arrival times of light propagating in the TE and TM modes, respectively. c,d) Absolute arrival time c) and slope d) of the TE and TM components extracted from UPMS experiments at different propagation distances in the waveguide, for a wavelength of 1550 nm . e,f) Linear group index dispersion obtained from the slopes of c,d) for TE e) and TM f) modes. Red lines indicate calculated group index using a numerical model (see Methods).

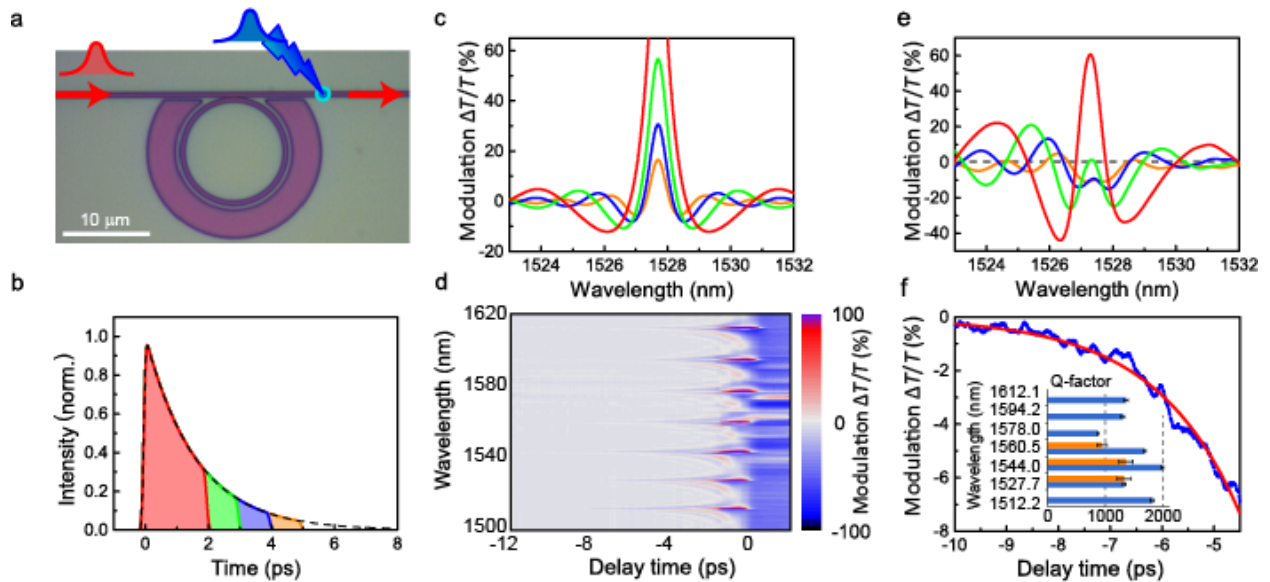


Fig. 4. Quality factor measurements in a ring resonator. a) Optical image of ring resonator structure with arrows showing arrangement for light incoupling and excitation. b,c) Calculated modulation spectra (c) assuming exponential ringdown (b, dashed black line) with ultrafast photomodulation gate included after 2 ps (red), 3 ps (green), 4 ps (blue) and 5 ps (orange). d) Delay time scan of change in transmission ($\Delta T/T$) of probe pulses on the output bus waveguide, shortly after the ring resonator. The scan shows the spectral features of the ring resonator at negative delay times, due to energy storage and ringdown. e) Slices through d) around $\lambda = 1523\text{-}1532$ nm and for delay times of -5 ps (orange), -4 ps (blue), -3 ps (green), and -2 ps (red). f) Modulation of resonance shown in e) against delay time. Red line indicates exponential decay fit with 1.63 ps photon dwell time in the ring resonator. Inset: histogram of quality factors obtained from UMPS experiments presented in d) (blue) and compared with quality factors from transmission measurements (orange).

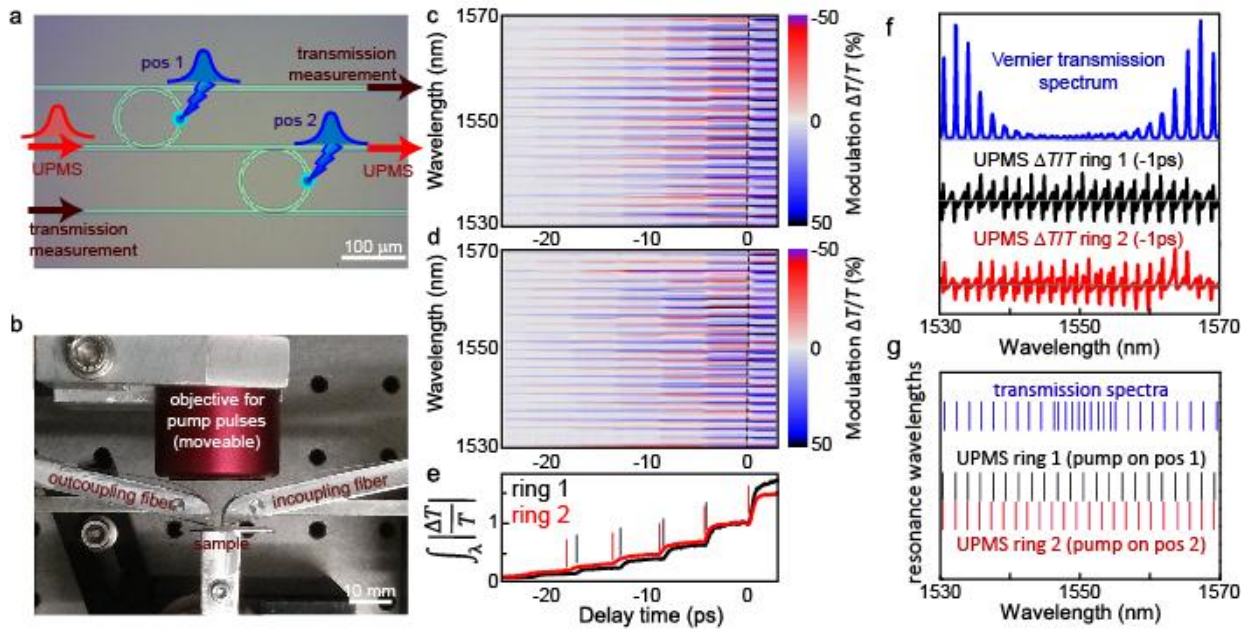


Fig. 5. Resonances of Vernier racetracks. a) Micrograph of Vernier structure with indicators for light incoupling and excitation. b) Photograph of setup with fibers for in- and outcoupling by grating couplers. c,d) UPMS measurements of the first (pump position 1) and second racetracks resonator (pump position 2), respectively. For easy comparison with (c), the graph in (d) has been shifted by 3ps. e) absolute value of the UPMS signal integrated over wavelength, reflecting the different round-trip times of the two resonators as indicated by the bars. f) Vernier transmission spectrum in comparison with the UPMS signal for both resonators at a delay time of -1ps. The three curves are shown in linear arbitrary units. g) Resonance wavelengths extracted from (f). Blue bars show the resonances as found from the Vernier transmission spectrum. Resonances from UPMS measurements of the individual racetracks are shown as black and red bars. The characteristics of the individual racetracks cannot be accessed by transmission measurements.

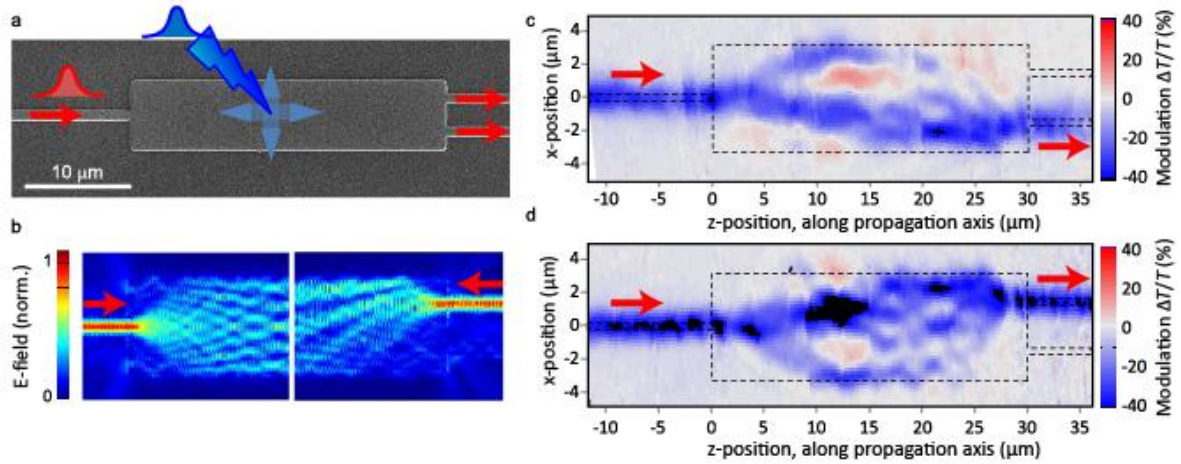


Fig. 6. Mode pattern mapping in a multimode interference (MMI) device. a) micrograph of the studied system. b) FDTD simulation intensity maps. In the left part, the incident wave is launched from the input waveguide. Areas of low intensity correspond to measurements presented in c,d. In the right part, the wave is incident from one output waveguide. The light paths contributing to this output are visible. c,d) UMPs measurements: spatial photomodulation maps of change in transmission ($\Delta T/T$) of probe pulses through the two outputs respectively, if the MMI is illuminated with the pump pulses at the position given by the map ($\lambda = 1556.5$ nm). The pump pulses arrive 4 ps before the probe pulses.